A Synthetic Signaling Network Imitating the Action of Immune Cells in Response to Bacterial Metabolism

Michal Walczak, Leonardo Mancini, Jiayi Xu, Federica Raguseo, Jurij Kotar, Pietro Cicuta, and Lorenzo Di Michele*

State-of-the-art bottom-up synthetic biology allows to replicate many basic biological functions in artificial-cell-like devices. To mimic more complex behaviors, however, artificial cells would need to perform many of these functions in a synergistic and coordinated fashion, which remains elusive. Here, a sophisticated biological response is considered, namely the capture and deactivation of pathogens by neutrophil immune cells, through the process of netosis. A consortium consisting of two synthetic agents is designed—responsive DNA-based particles and antibiotic-loaded lipid vesicles—whose coordinated action mimics the sought immune-like response when triggered by bacterial metabolism. The artificial netosis-like response emerges from a series of interlinked sensing and communication pathways between the live and synthetic agents, and translates into both physical and chemical antimicrobial actions, namely bacteria immobilization and exposure to antibiotics. The results demonstrate how advanced life-like responses can be prescribed with a relatively small number of synthetic molecular components, and outlines a new strategy for artificial-cell-based antimicrobial solutions.

1. Introduction

Recent years have witnessed a substantial growth in the fields of artificial cell science and bottom-up synthetic biology,[1–6] which aim at producing cell mimics capable of replicating the behaviors of biological cells. Artificial cells hold applicative potential in diagnostics[7] and therapeutics,[8–11] as well as in fundamental biology[12] and origin of life research.[13] This interest has led to a rapid expansion of the available design toolkit for artificial cells,

enabling replication of biological processes and features such as division,[14–16] metabolism,[17,18] growth,[19] motility,[20,21] communication,[22,23] sensing,[24,25] compartmentalization,[26–28] protein expression,[29] and DNA replication.[30] Artificial cells have been successfully built from membrane-bound scaffolds in the form of liposomes,[31,32] polymersomes[31,33] and proteinosomes,[34,35] as well as from membrane-less coacervates or hydrogels.[27,36–39]

While these early successes in mimicking individual biological functions carry both applicative and fundamental interest, challenges remain in place when attempting to design artificial cells capable of sustaining more advanced biomimetic responses, where many elementary functions need to be performed in a coordinated way. Among the advanced behaviors we seek to implement are those that resemble the action of the immune system,[40,41] which would unlock disruptive applications of artificial cells to in vivo therapeutics.[42] In this scenario, artificial cells would need to establish multiagent signaling and signal transduction networks with biological and other artificial cells, involving several interlinked responses: i) detection and transduction of signals generated by live cells; ii) communication with live cells and possibly other artificial cells; iii) information processing; iv) individual and/or collective responses that may involve both physical and chemical action, for example, the release of therapeutic agents and the mechanical perturbation of live cells.

M. Walczak, L. Mancini, J. Xu, J. Kotar, P. Cicuta, L. Di Michele
Biological and Soft Systems
Cavendish Laboratory
University of Cambridge
JJ Thomson Avenue, Cambridge CB3 0HE, UK
E-mail: ld389@cam.ac.uk

J. Xu, L. Di Michele
Department of Chemical Engineering and Biotechnology
University of Cambridge
Philippa Fawcett Drive, Cambridge CB3 0AS, UK

F. Raguseo, L. Di Michele
Department of Chemistry
Molecular Sciences Research Hub
Imperial College London
Wood Lane, London W12 0BZ, UK

F. Raguseo, L. Di Michele
fabriCELL
Molecular Sciences Research Hub
Imperial College London
Wood Lane, London W12 0BZ, UK

**ADVANCED
SCIENCE NEWS**

www.advancedsciencenews.com
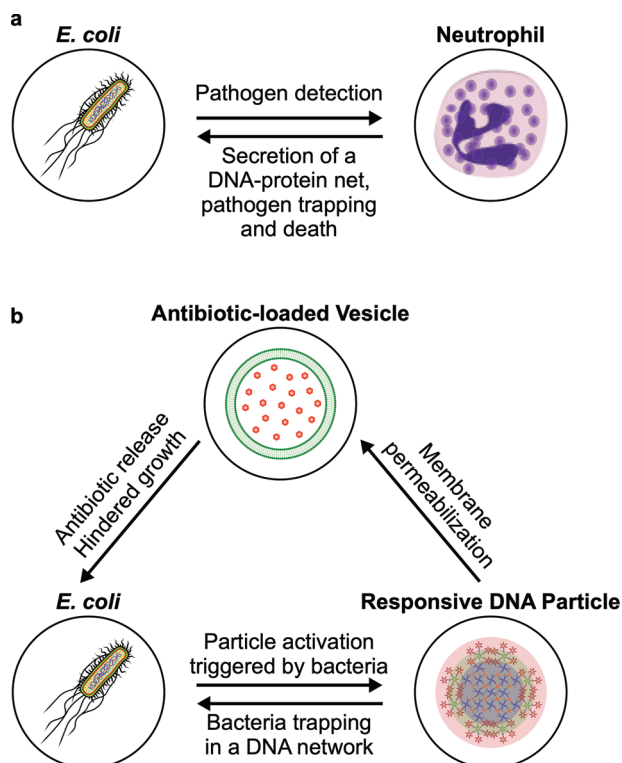
**ADVANCED
MATERIALS**

www.advmat.de

Figure 1. Three-agent synthetic consortium mimics the antimicrobial response of innate immune cells. a) Neutrophils respond to the presence of pathogens by excreting a mesh formed by their genomic DNA, histones, and granules containing molecules with antimicrobial properties. The neutrophil extracellular trap (NET) immobilizes the pathogens and kills them due to the antimicrobial properties of the molecules associated. b) Three-agent synthetic consortium designed to exhibit a netosis-like response. Responsive DNA-based particles detect model targets (*E. coli*) by sensing medium acidification induced by the glucose metabolism of the cells. "Activated" particles respond by forming a sticky DNA–cholesterol network that immobilizes the bacteria and, at the same time, permeabilizes antibiotic-loaded giant unilamellar vesicles (GUVs). Antibiotic release suppresses bacterial growth and division, fulfilling the antimicrobial role of the DNA-binding proteins in the biological system.

Successful attempts at establishing signaling networks between live and artificial cells have been reported, often involving one-way communication, for example, triggering of bacterial gene expression,[43–50] and more rarely two-way pathways leading to cell death.[10] However, these remarkable examples are still relatively simple, relying on one or a small number of individual functionalities, and thus failing to address the need to engineer more advanced emerging behaviors.

In this contribution, we aim to build a synthetic signaling network that mimics a complex response of the innate immune system, namely that of netosis,[51–53] whereby neutrophils excrete a sticky neutrophil extracellular trap (NET) formed from their genomic DNA, which traps pathogens and then disrupts them thanks to embedded antimicrobial proteins (**Figure 1**a). As sketched in Figure 1b, the synthetic pathway we propose features two artificial-cell-like agents, i) responsive DNA-based particles[54] and ii) antibiotic-loaded liposomes, whose coordinated action, triggered by bacterial activity, gives rise to the

sought behavior. The DNA-particles sense a decrease in pH resulting from the natural glucose metabolism of *Escherichia coli*,[55] and respond by exposing their hydrophobic core, which then leads to the formation of a synthetic DNA NET. The sticky material traps and immobilizes the bacteria and, at the same time, permeabilizes the liposomes, which ultimately release an antibiotic able to hinder growth of the trapped cells. The synthetic netosis pathway coordinates several functionalities, including one-way (particles → liposomes and liposomes → bacteria) and two-way (particles ↔ bacteria) communication, a collective self-assembly response, and both physical and chemical interference with bacterial activity. Our proof-of-concept implementation thus demonstrates how advanced life-like behaviors can be engineered from the bottom-up, relying on a relatively small number of molecular and nanoscale components. In addition, the platform represents a starting point for the development of biomimetic antimicrobial solutions and, more generally, synthetic-cell therapeutics.

2. Results and Discussion

2.1. Fabrication of pH-Responsive DNA Particles

Figure 2a shows the DNA-based particles used in this work, which feature a core–shell structure with an hydrophobized center surrounded by an hydrophilic outer layer, the latter ensuring colloidal stability. The amphiphilic core motifs (CM) consist of 4-pointed DNA junctions (nanostars), with the end of each double-stranded (ds) DNA arm labeled by a cholesterol moiety. Similar "C-star" designs have been shown to self-assemble into framework-like materials sustained by cholesterol-mediated hydrophobic forces, with programmable nanoscale morphology and multi-stimuli-responsiveness.[27,54,56–58] The shell comprises of two 6-pointed all-DNA nanostars, labeled as inner and outer corona motifs (ICM and OCM, respectively), together forming dendrimeric construct that can connect to core motifs through single-stranded (ss) DNA overhangs (Figure 2a). As we recently demonstrated, the core–shell particle morphology can be attained following a two-step thermal annealing process, which can be adapted to prescribe the size of the particles, from a few hundred nanometers to several micrometers.[54] Figure 2b shows a large particle where the sought core–shell structure is clearly visible in confocal microscopy. Particles of this large size were purposefully created with a modified assembly protocol to enable facile confocal visualization. For the remainder of this work, the assembly protocol was set up to produce smaller particles, with hydrodynamic radius of either ≈1 μm, ≈750 nm, or ≈200 nm, depending on the specific experiment. Details of sample preparation are provided in Experimental Section, while sequences of all oligonucleotides used in the work and composition of all samples are shown in Tables S1 and S2, Supporting Information, respectively. Correct assembly of the individual core and corona motifs was verified with both agarose gel electrophoresis (AGE) and dynamic light scattering (DLS), summarized in Figures S1 and S2, Supporting Information, while their thermal stability was assessed with UV-absorbance (Figure S3, Supporting Information). In our previous contribution, we have demonstrated that removal of the corona, induced by a non-biologically relevant ssDNA
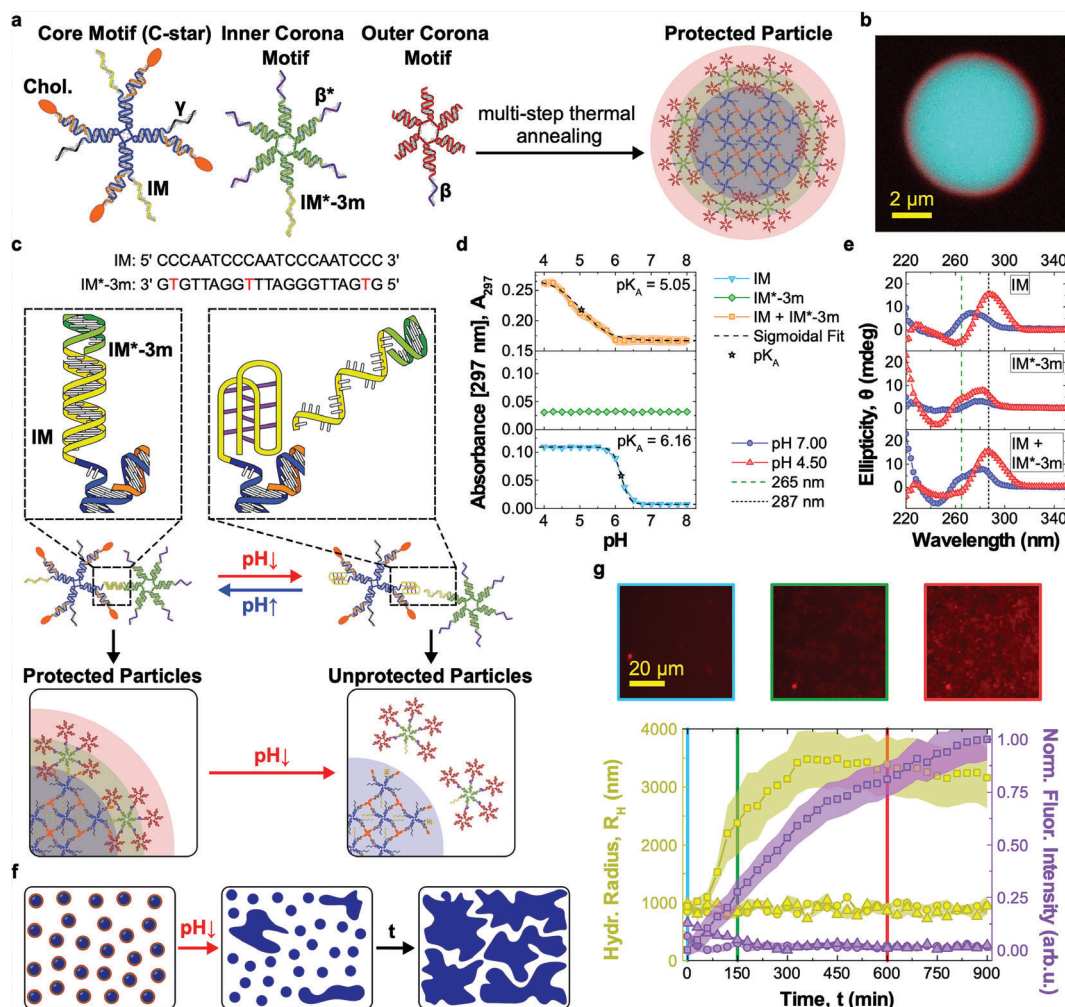
Figure 2. Core–shell DNA-based particles form a network in response to pH changes. a) Core–shell DNA particles assemble from cholesterolized (core motifs, CMs) and non-cholesterolized DNA nanostars (inner and outer corona motifs, ICM, and OCM, respectively).[54] CMs, composed of cholesterol-functionalized (orange) and non-functionalized strands (blue), form the hydrophobic particle core. ICMs and OCMs create a stabilizing corona. CMs and ICMs bind through domains *IM* and *IM*-3m*, while ICMs and OCMs attach through $\beta-\beta^*$ overhangs. Domain γ can be used to fluorescently label CMs, by connecting to an Alexa Fluor 594-labeled duplex. When not used, γ is replaced by a poly-T sequence. Sequences of all strands used in this work and composition of all samples are outlined in Tables S1 and S2 (Supporting Information), respectively. The relative thickness of core and shell region in the schematics is not in scale. b) Confocal microscopy image of a large particle with distinguishable core–shell structure, assembled through a slow annealing protocol. Particles used in the remaining experiments had a much smaller size (200 nm to 1 µm, see Experimental Section). CMs are shown in cyan (fluorescein), OCMs in red (Alexa Fluor 647). c) *IM* and *IM*-3m* domains are designed to cause the detachment of ICMs from CMs at low pH. *IM* is C-rich, able to form a non-canonical i-motif under acidic conditions,[59] resulting in destabilization of the duplex formed by *IM* and *IM*-3m*. The duplex is rendered less stable by mismatches between the two sequences (red). d) pH-dependence of the UV absorbance at 297 nm, measured as proxy for i-motif formation,[60,61] for samples of *IM*, *IM*-3m*, and *IM* + *IM*-3m* oligonucleotides (not linked to star motifs). Increase in A_{297} marks i-motif formation achieved at pH ≈6.16 for isolated *IM* and ≈5.05 when also *IM*-3m* is present, with the difference ascribed to competition between duplex and i-motif formation. The transitional pH (pK_A) values were calculated as the inflection points of sigmoidal fits. No response was observed in isolated *IM*-3m*. The data are shown as mean ± standard error (shaded regions) of two experiments performed on two independently prepared samples, each consisting of three measurements. e) Circular dichroism (CD) spectra of the samples in (d) Characteristic maxima at 287 nm and minima at 265 nm[60,61] confirm i-motif formation in *IM* and *IM* + *IM*-3m* samples. Data are averaged over three measurements. f) Schematic representation of pH-induced particle aggregation. pH decrease leads to i-motif formation, corona displacement, exposure of the sticky cholesterol–DNA cores, and ultimately particle aggregation. g) Bottom: particle aggregation after pH decrease tracked by measuring the hydrodynamic radius of growing aggregates with differential dynamic microscopy (DDM, left axis)[62,63] and the normalized epifluorescence intensity of accumulating CMs labeled with Alexa Fluor 594 (red, right axis). Triangles and squares represent responsive particles incubated at pH 7.0 (triangles) and 4.5 (squares). Circles indicate a control sample with nonresponsive particles at pH 4.5, where the *IM* and *IM*-3m* domains have been replaced with non-responsive sequences. Data are plotted as mean ± standard error (shaded regions) of three (circles and triangles) or six (squares) measurements conducted on two independently prepared samples. Top: epifluorescence microscopy images of responsive particles after pH decrease at different time points (*t* = 0, 150, and 600 min). See Figure S5, Supporting Information for additional microscopy images.

trigger, leads to exposure of the particles' hydrophobic cores and formation of a sticky DNA–cholesterol network.[54] The network has then been shown to trap motile *E. coli* and, independently, disrupt giant unilamellar lipid vesicles (GUVs).[54] These are two key functionalities for the netosis-like signaling network we seek to implement here (Figure 1b). However, multiple critical features are missing from the system presented in ref. [54], including the ability of the particles to directly respond to signals generated by the target cells.

Establishing this missing communication link requires the identification of a sufficiently general, cell-generated signal that can be coupled with the reconfiguration of the DNA nanostructures. Our model target—*E. coli*—similar to several other species, is well known to naturally acidify its microenvironment as a result of its sugar metabolism.[55] We thus identified pH as the ideal biogenous trigger, and proceeded to render the particles pH-responsive, so that the protective corona detaches from the sticky core at sufficiently low pH. This effect was obtained by engineering the DNA overhangs that link the CMs to the ICMs, and in particular by exploiting the pH-responsiveness of C-rich sequences. As highlighted in Figure 2c, at neutral pH ($\approx$7), the C-rich *IM* domain[59] on the CM hybridizes to domain *IM*-3m* on the ICM, due to them being complementary but for three base mismatches. At lower pH, the duplex formed by *IM* and *IM*-3m* is destabilized by the formation of an intra-molecular, non-canonical i-motif in *IM*,[59,61,64] thus leading to separation of the CM from the ICM.

We characterized the pH-induced i-motif-to-duplex transition by recording UV absorbance at 297 nm, known to increase following C-protonation and i-motif formation.[60,61] Results, collated in Figure 2d, show a transitional pH value (pK_A) equal to 6.16 for samples that only contain *IM*, which is reduced to 5.05 when also *IM*-3m* is present, owing to duplex hybridization counteracting i-motif formation. A similar pK_A was obtained with Dynamic Light scattering (DLS) measurements assessing the pH-dependent complexation of CMs and ICMs, as shown in Figure S4, Supporting Information. i-motif formation was further confirmed by Circular dichroism (CD), as summarized in Figure 2e. At pH 4.50, samples containing *IM*, both with and without *IM*-3m*, produced CD spectra with a maximum at 287 nm and minimum at 265 nm, both characteristic of the i-motif.[60] In traces recorded at pH 7.00, both extremes were shifted to lower wavelengths, as expected for dsDNA.

pH-induced corona displacement causes the exposure of the particles' sticky cores, leading to their cholesterol-mediated aggregation and the formation of an extended amphiphilic DNA network, as shown in Figure 2f. To assess network formation we used DDM,[62,63] which allowed the monitoring of the time-evolution of the hydrodynamic radius of the particles, R_H, after lowering the pH to 4.5. The data, collated in Figure 2g (left axis, squares), show the expected increase in R_H from the initial value of $\approx$1 μm, resulting from particle aggregation. Network formation is visible in epifluorescence microscopy images collected using particles labeled with Alexa 594 (Figure 2g, top). The mean (normalized) fluorescence intensity from the microscopy images can further be used to track particle aggregation, exploiting progressive sedimentation of the aggregates that leads to an increase in the fluorescent signal close to the bottom of the imaging well. The fluorescence traces shown in Figure 2g (right axis, squares),

expectedly, follow a trend similar to the hydrodynamic radius. To confirm the specificity of the observed aggregation response, we conducted two control experiments, one in which pH responsive particles were kept at pH 7 (triangles) and another where non-responsive particles, obtained by replacing the C-rich motif with a sequence unable to form an i-motif, were exposed to pH 4.5 (circles). In both controls, no aggregation was noted from the R_H or fluorescence intensity data (Figure 2g), confirming that the observed network formation indeed emerges from the designed pH-responsive pathway. The absence of non-triggered aggregation, also confirmed for different medium compositions (Figure S6, Supporting Information), demonstrates the stability of the particles in bare media over experimentally relevant timescales. An extended set of bright-field and epifluorescence microscopy images, showing the behavior of responsive/nonresponsive particles at neutral and acidic pH, is included in Figure S5, Supporting Information.

2.2. Bacteria Immobilization Triggered by Glucose Metabolism in *E. coli*

Acidification of the extracellular milieu is a very common phenomenon, as a vast number of microorganisms produce acids as a consequence of fermentative processes. Particularly notable among them are bacteria belonging to the Bacillota and Pseudomonadota phyla that include human pathogens such as *Pseudomonas aeruginosa*, *Enterococcus faecalis*, *Salmonella enterica*, *Streptococcus pneumoniae*, *Yersinia pestis*, and *E. coli*.[55] Due to its high tractability in lab settings, we set out to demonstrate our synthetic netosis-like pathway in the presence of *E. coli*, which excretes acetate as a result of glucose metabolism thereby acidifying its growth medium, as sketched in **Figure 3**a. Having designed responsive DNA-based particles capable of forming a sticky network upon exposure to acidic conditions, we proceed to determine whether: i) the particles can be "activated" by glucose metabolism in *E. coli* and ii) the formed network can trap the cells, as required for the synthetic netosis-like response outlined in Figure 1 (right).

As demonstrated in Figure 3b (left), the magnitude of the pH decrease in *E. coli* cultures can be modulated by changing the initial concentration (ρ_G) of glucose in the medium. For all but the lowest tested glucose concentrations (0.001% and 0.01% w/v) a notable decrease in pH was observed, followed by a recovery for $\rho_G \leq 0.200$% w/v due to re-uptake of acetate at later growth stages.[55] The magnitude of the pH drop correlates with glucose concentration, with values lower than 5, required for particle activation, reached when $\rho_G \gtrsim 0.150$% w/v. Figure 3b (right) explores the link between glucose concentration and cell growth, quantified through optical density (600 nm). The highest yield was observed for $\rho_G = 0.150$% w/v, with lower yields noted for both higher and lower ρ_G values. The substantially lower yield seen at high ρ_G (0.300% w/v) correlates with the lack of recovery in pH observed in Figure 3b (left), hinting that excessive acidification may impact *E. coli* metabolism and prevent acetate re-uptake. In Figures S7 and S8, Supporting Information we present OD and pH data collected for *E. coli* cultured in well plates, relevant for the synthetic netosis experiments discussed below (see Experimental Section). Trends similar to those reported in Figure 3b
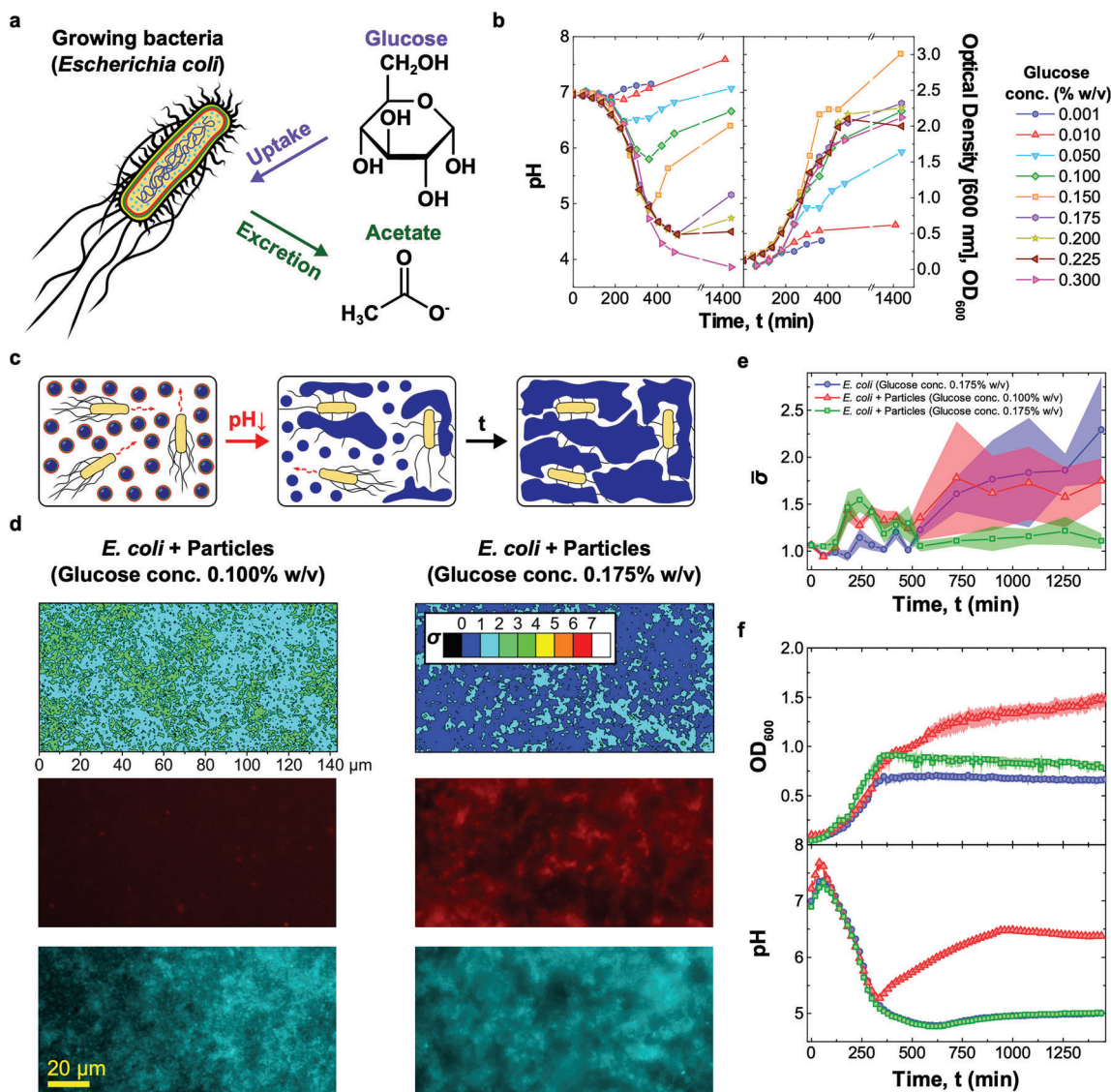
Figure 3. pH-responsive DNA particles trap *E. coli* when triggered by bacterial metabolism a) Glucose metabolism in *E. coli* leads to acetate release and pH decrease.[55] b) (left) Bacteria-induced pH changes depend on glucose concentration in the medium, ρ_G. For intermediate values (0.050% w/v $\leq \rho_G \leq$ 0.200% w/v) the pH decreases and reaches a minimum before recovering. For $\rho_G \geq$ 0.225% w/v recovery is not observed. Glucose concentration influences bacterial growth, quantified through turbidity (OD) measurements at 600 nm (right). Culture yield increases with ρ_G, is maximized at intermediate values, and decreases at higher glucose concentration, possibly due to excessive medium acidification. Data for ρ_G = 0.175, 0.200, and 0.225% w/v are shown as average of three independent repeats, the remaining points are from a single repeat. c) Diagram illustrating *E. coli* trapping by the synthetic DNA net. Bacterial metabolism reduces the pH, causing particle activation and the formation of a sticky network (Figure 2) that embeds the cells. d) (top) *E. coli* immobilization induced by DNA net formation as quantified through the motility parameter σ, extracted from bright-field microscopy videos (see Experimental Section). The two colormaps are relative to samples containing *E. coli*, responsive particles and different ρ_G values, one insufficient (0.100% w/v, left) and the second sufficient (0.175% w/v, right) to reach the pH threshold for particle activation (5.05, see Figure 2d). Bottom: epifluorescence microscopy images corresponding to the σ-maps. Core motifs are labeled with Alexa Fluor 594 (red), while *E. coli* express EGFP (cyan). Smaller σ-values and co-localization of DNA and bacteria observed in the sample with higher glucose concentration confirm the ability of cholesterol–DNA networks to bind and immobilize *E. coli*. σ-maps and images were collected at t = 1440 min after sample preparation. e) Time evolution of the frame averaged motility parameter $\bar{\sigma}$ recorded for the samples in (d) and a control sample with *E. coli* and ρ_G = 0.175% w/v, but lacking DNA particles. The decrease in $\bar{\sigma}$ noted in the sample with responsive particles and higher glucose concentration confirms reduced *E. coli* motility following trapping. Data are shown as mean ± standard error of seven measurements conducted on three independent repeats. Associated σ-maps and epifluorescence microscopy images are shown in Figure S11, Supporting Information. f) Time-traces of OD (top) and medium pH (bottom) for the three samples in (e). The pH was measured using the ratiometric pH probe FITC-dextran, added in solution (see Figures S9 and S10, Supporting Information, and Experimental Section). For both OD and pH, data are shown as averages of three independent repeats. For the OD curves, standard errors are shown as shaded regions.

for flask cultures were noted, both in terms of growth curves and pH traces. A systematic difference was observed in the lowest pH reached for $\rho_G = 0.300\%$ w/v, which was higher in well plates compared to flask experiments (≈ 4.75 and ≈ 4, respectively). This deviation is likely due to the different method used to record pH, which relied on a physical pH probe in flasks and on a ratiometric fluorescent probe, FITC-dextran, in well plates. The response of the fluorescent probe was indeed found to saturate at pH ≈ 5 (Figure S9, Supporting Information). We note that, to preserve the buffer conditions optimized for particle assembly and stability, bacteria were cultured in a newly developed medium dubbed PBM9. Medium composition, outlined in Experimental Section, was selected to match ionic and buffering properties of phosphate-buffered saline (PBS) buffer and contain compounds needed to support bacterial growth, as in the M9 medium.

Having characterized the ability of *E. coli* to acidify their medium, we proceeded to test DNA-particle activation and consequent bacteria trapping. As sketched in Figure 3c, the pH-responsive particles were deployed in *E. coli* samples with $\rho_G = 0.175\%$ w/v, sufficient to achieve the pH-level required for particle activation, and $\rho_G = 0.100\%$ w/v, insufficient to reach the threshold (compare Figure 2d (top) and Figure 3b (left)). We note that the two ρ_G values result in comparable growth rates (Figure 3b, right).

Epifluorescence images of both particles (red) and bacteria (cyan), collected after incubating the samples for $t = 1440$ min, are shown Figure 3d (bottom). The snapshots readily demonstrate formation of the synthetic DNA net in the sample with higher glucose concentration, while no visible particle aggregation was seen for $\rho_G = 0.100\%$ w/v. We can thus confirm that metabolism-induced acidification is capable of triggering particle aggregation, establishing the sought communication link between the cells and the synthetic DNA constructs. To assess whether the DNA net displays the desired ability to trap motile *E. coli*, a parameter σ was extracted from high-framerate bright-field microscopy videos of the samples, defined as the time-averaged standard deviation of the pixel-intensity computed over seven consecutive frames (see Experimental Section). We have previously demonstrated that σ represents a good proxy for bacterial motility, taking larger values in samples of motile *E. coli* and lower values if the cells are immobilized.[54] A clear difference in σ between the sample with lower and higher ρ_G is notable from the colormaps in Figure 3d (top), relative to the end-point of our experiments ($t = 1440$ min). The substantial reduction in bacterial motility observed for $\rho_G = 0.175\%$ w/v confirms that the DNA-particles were able to trap *E. coli*, once activated by the bacteria themselves, hence confirming two-way particle–cell communication.

The relative homogeneity of σ across the fields of view allows us to track the time evolution of bacteria motility by monitoring the frame-averaged $\bar{\sigma}$, as summarized in Figure 3e for the two samples discussed in Figure 3d. A control *E. coli* sample with $\rho_G = 0.175\%$ w/v, but lacking DNA particles, is also included. After initial fluctuations, $\bar{\sigma}$ increases in the sample with $\rho_G = 0.100\%$ w/v and in the control sample, as a result of the increase in number of cells (compare Figure 3b) and the lack of physical constraints limiting their motility. In contrast, in the sample containing particles, under conditions supporting their activation ($\rho_G = 0.175\%$ w/v), $\bar{\sigma}$ decreases at $t = 510$ min min before plateauing at $t = 720$ min, as a consequence of DNA net formation and bacteria trapping. The onset of net formation correlates with the time-evolution of the pH reported in Figure 3f (bottom), showing that the pH threshold required for particle activation (5.05) was reached prior to the time at which $\bar{\sigma}$ decreased. pH data were recorded with the fluorimetric probe FITC-dextran. See Figures S9 and S10, Supporting Information, for the calibration curve and raw fluorescence data, respectively. Both the pH trends and the OD growth curves shown in Figure 3f (bottom and top, respectively) closely match data collected in samples lacking particles (Figure S8, Supporting Information), indicating that particles have negligible effect on bacterial growth and metabolism under the tested conditions. Epifluorescence images and σ colormaps for the three samples discussed in Figure 3e,f are shown in Figure S11, Supporting Information, for selected time-points, enabling visual assessment of the difference in sample evolution resulting from net formation and bacteria trapping.

The modularity of our DNA nanodevices allowed us to introduce additional functionality in the bacteria-trapping DNA particles. This is exemplified in Figures S12 and S14 (Supporting Information), where we tested design variations of the particles that enable in situ fluorescent reporting of the bacteria-induced pH change, and consequent particle activation. In Figure S12, Supporting Information, pH sensing was achieved by linking the ratiometric pH probe FITC-dextran to the core motifs. Observed trends were similar to the ones obtained with probes freely diffusing in bulk (Figure 3f and Figure S10, Supporting Information), but with the advantage that the labeled particles can probe pH in the local DNA-net microenvironment, in the vicinity of trapped bacteria. See also the calibration curve in Figure S13, Supporting Information. In Figure S14 (Supporting Information), instead, we detected the pH-induced detachment of the corona motifs from the core motifs by placing a fluorophore and quencher on the *IM* and *IM*-3m domains, respectively. The biosensing capabilities of the material could be potentially further expanded by including agents that monitor alternative metabolic processes, for example, Fe(III) respiration metabolism, as reported by Chen et al.[65]

2.3. Bacterial Growth Inhibition Induced by the Synthetic Netosis-Like Pathway

With the pH-responsive DNA particles we have successfully replicated two of the key responses of netosis, namely the detection of target cells and their immobilization in a sticky DNA–cholesterol network. One last property is missing to fully mimic the biological response, and that is the antimicrobial action of the neutrophil extracellular traps causing cell death in the trapped pathogens. As observed above, however, the synthetic cholesterol–DNA net does not suppress bacterial growth under the tested conditions. Hence, to endow the system with antimicrobial properties, we introduced a second synthetic agent: a GUV loaded with the antibiotic ciprofloxacin, as sketched in Figure 1b. The antibiotic was chosen due to its low minimum inhibitory concentration (MIC, Figure S15, Supporting Information), and encapsulated within the GUVs at $200\times$ this value (3.2 µg mL^{-1}). The designed netosis-like response of the resulting three-agent artificial consortium is graphically outlined in **Figure 4**a: after

**ADVANCED
SCIENCE NEWS**
www.advancedsciencenews.com
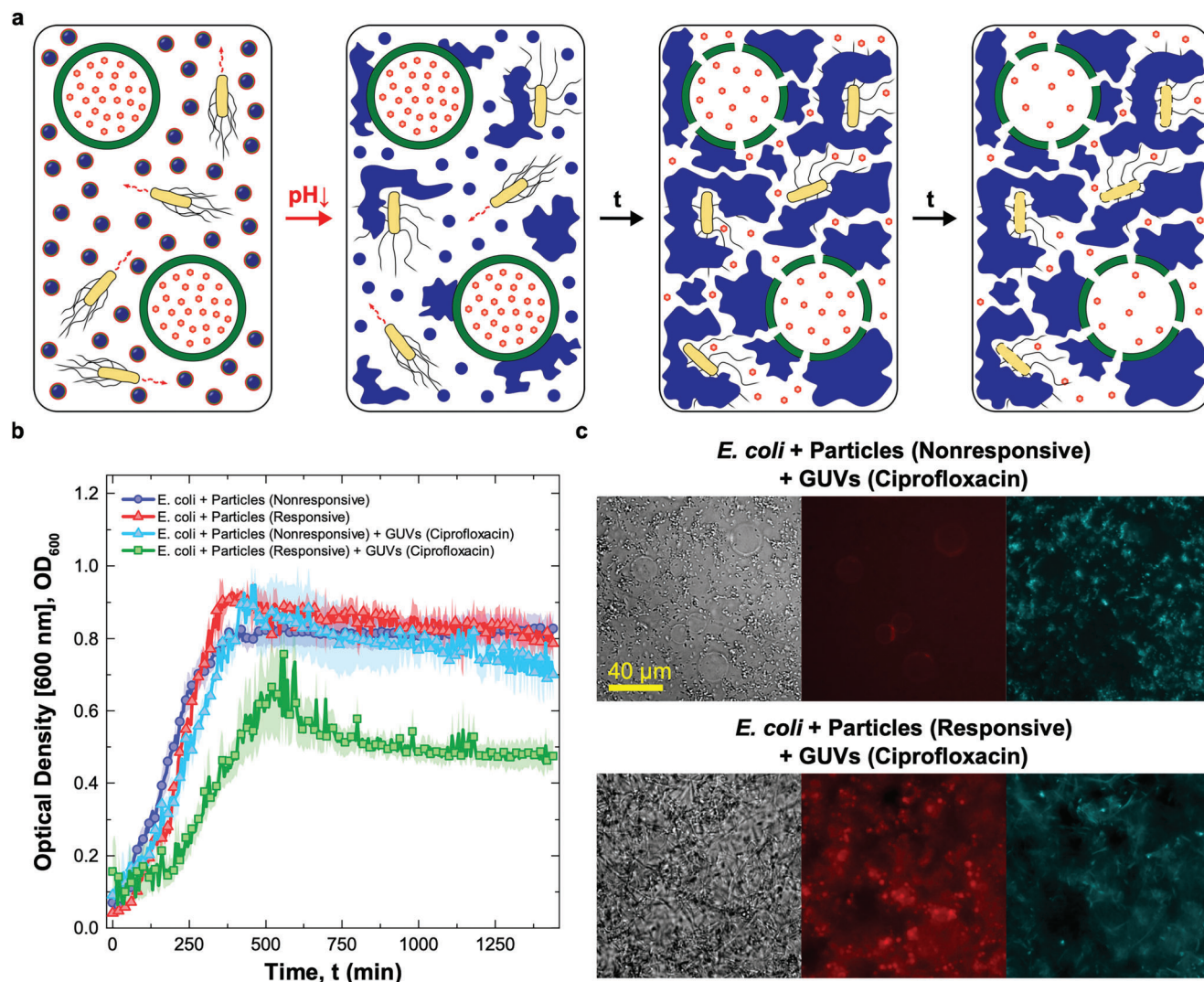
**ADVANCED
MATERIALS**
www.advmat.de

Figure 4. Synthetic cell signaling network produces netosis-like response a) Diagram illustrating the mechanism of action of the synthetic signaling network producing a netosis-like response. Medium acidification caused by *E. coli* glucose metabolism activates the DNA-particles. The particles form a sticky DNA–cholesterol network that, simultaneously, traps the bacteria and permeabilizes giant unilamellar vesicles (GUVs) loaded with antibiotic ciprofloxacin. The released antibiotic hinders bacterial growth. b) Antimicrobial response as determined via turbidity measurements (OD at 600 nm). Data are shown for four samples as the mean of three independent repeats ± standard errors (shaded regions). One sample includes *E. coli*, antibiotic-loaded GUVs, responsive particles, and sufficient glucose to achieve their activation ($\rho_G = 0.175\%$ w/v), and is thus capable of supporting the cascade of reactions producing the sought netosis-like response (green squares). The other tree samples are controls missing one or more key components. Two control samples lack antibiotic-loaded GUVs, and feature either non-responsive (blue circles) or responsive (red triangles) DNA particles. The third control sample contains antibiotic-loaded GUVs but uses non-responsive particles. While all control samples show similar OD curves, growth is delayed and suppressed in the system capable of sustaining the designed cascade of reactions. c) Bright-field and epifluorescence microscopy images of samples containing *E. coli*, nonresponsive (top) or responsive (bottom) particles and ciprofloxacin-loaded GUVs, recorded at $t = 1440$ min after sample preparation. Aggregation of DNA and the lack of GUVs in the sample with responsive particles indicates the successful rupture of vesicles following DNA-net formation. The released antibiotic hinders *E. coli* division, causing cell elongation. Particles (core motifs) are shown in red (Alexa Fluor 594), *E. coli* in cyan (EGFP). See Figure S16, Supporting Information for additional bright-field and epifluorescence microscopy images recorded at $t = 0$ and 1440 min.

E. coli-induced medium acidification, the unprotected particles are expected to bind to the GUV and either disrupt or permeabilize them, causing the release of the drug that would, in turn, hinder the growth of trapped bacteria. The ability of unprotected cholesterol–DNA particles to render GUVs permeable has been tested in our previous contribution, using a fluorescent probe.[54]

To evaluate the antimicrobial action of the drug-loaded GUVs, and thus validate the netosis-like response of our synthetic consortium, we conducted an assay in which GUVs and pH-responsive particles were deployed in an *E. coli* sample along with 0.175% w/v glucose, sufficient to induce particle activation thorough medium acidification (Figure 3). The resulting OD growth curve is shown in

**ADVANCED
SCIENCE NEWS**

www.advancedsciencenews.com

**ADVANCED
MATERIALS**

www.advmat.de

Figure 4b (green squares), and compared with data from three distinct control experiments where we selectively eliminated components and functionalities required for the antimicrobial response. These include samples in which GUVs were not present and particles were either non-responsive (blue circles) or pH-responsive (red triangles), or where the GUVs were present along with non-responsive particles (cyan triangles). All control experiments produced similar growth curves, providing a baseline and confirming that neither the particles (responsive or nonresponsive), nor undisturbed antibiotic-loaded GUVs, influence growth. The sample sustaining the complete netosis-like pathway, instead, produced a visibly different response. While growth is similar to the controls in the initial two hours, once acidification and consequent particle activation occur, growth slows down leading to a maximum OD lower compared to the controls, followed by a noticeable decrease in OD at later times. A visual insight in the response of the systems can be gained from the bright-field and epifluorescence images in Figure 4c, collected at the end of the experiments (t = 1440 min from sample preparation). Here, the control sample featuring GUVs and non-responsive particles is compared with the complete netosis-like system. In the control, no DNA net was formed (red epifluorescence channel) and the GUVs clearly retained their structural integrity (bright field) despite weak interactions with the non-activated particles (red channel). Bacteria also retained their physiological rod-like shape (bright-field and cyan epifluorescence channel). Instead, in the sample capable of sustaining the full cascade of reactions leading to netosis, GUVs were no longer visible, having been disrupted by the formed DNA net. The consequent release of antibiotic had a clear effect the ability of *E. coli* to divide, as the cells acquired a visible filamentous morphology. The microscopy data, along with additional images provided in Figure S16 (Supporting Information) confirm the ability of our synthetic consortium to sustain the designed responses leading to the sought netosis-like mechanism.

3. Conclusion

We have reported the bottom-up construction of a synthetic signaling network capable of imitating a complex immune response, namely that of netosis. Through this process, neutrophils detect, trap, and kill pathogens by secreting a DNA-based extracellular trap. Our artificial netosis pathway relies on the action of DNA-based synthetic particles, which upon detecting bacteria-induced medium acidification, form a sticky network reminiscent of the biological trap, capturing the cells. Simultaneously, the particles cause antibiotic to be released from liposomes, hindering growth and division in the trapped cells.

The netosis-like behavior emerges from the coordinated activation of multiple biomimetic functions, including biosensing, morphological adaptation, and communication, exemplifying how advanced life-like responses can be implemented with a relatively small number of molecular components, exploiting the modularity and programmability of nucleic-acid nanotechnology. Inspired by our solution, similar synthetic pathways could be implemented to program responses in the bacterial communities different from their death, for instance by load-

ing the liposomes with inducers triggering protein synthesis,[50] exploiting the cell-trapping functionality to engineer multi-species microbial consortia,[66] or scaffolding synthetic biofilms, valuable in biomaterial synthesis[67] and bioremediation.[68,69] The resulting "living biomaterials",[70] may also feature rheological properties which are dependent on the activity of the trapped cells, deserving future investigation.[71] Matrix rheology could, in turn, influence cell growth,[72] enabling the design of adaptable materials reliant on biomechanical feedback loops.

Besides pushing the boundaries of bottom-up synthetic biology, our implementation could underpin disruptive antimicrobial solutions that, like our natural immunity, benefit from the combination of physical (cell immobilization) and chemical (antibiotics) modes of action. To this end, activation of the synthetic net could be rendered conditional to pathogen-associated stimuli other than pH, such as the presence of cell-surface antigens[73] or soluble biomarkers,[74] exploiting base-paring, aptamer technology or functionalization with chemical or biological ligands. Solutions could also be devised to integrate the cargo-loaded liposomes and DNA-particles in a single agent, exploiting well-established strategies to link DNA devices to lipid membranes.[75,76] The resulting "synthetic immune cell" could be valuable beyond antimicrobials, and be adapted to tackle, for example, inflammation or cancer by adjusting the therapeutic payload and trigger stimulus, building toward the ambitious goal of creating effective and robust synthetic cellular therapies.[42]

4. Experimental Section

Design and Handling of DNA Strands: DNA nanostructures were designed in NUPACK.[77] A constraint forbidding more than three consecutive C or G bases was imposed to inhibit formation of unwanted secondary structures. The i-motif forming domain and its complement were excluded from this constraint. All sequences are provided in Table S1, Supporting Information. Core Strand 1, carrying the internal rhodamine 6G modification was purchased from Eurogentec. All remaining strands were bought from Integrated DNA Technologies (IDT). The functionalized and non-functionalized oligonucleotides were purified by the supplier using high-performance liquid chromatography and standard desalting, respectively. Once delivered, the dehydrated DNA was reconstituted in PBS (137 mM NaCl, 2.7 mM KCl, 8 mM Na_2HPO_4, 2 mM KH_2PO_4, pH 7.4, Invitrogen, Thermo Fisher Scientific). To remove any large particulate contaminants the solutions of non-functionalized oligonucleotides were syringe-filtered with polyethersulfone filters (0.22 μm pore size, Millex). The concentration of reconstituted DNA samples was determined by measuring the absorbance at 260 nm on a Thermo Scientific Nanodrop 2000 UV–vis spectrophotometer. The extinction coefficients were provided by the supplier (IDT) or calculated using the OligoAnalyzer online tool from IDT. All stock solutions were stored at −20 °C.

Preparation of Non-Functionalized DNA Structures: Samples used to probe the folding efficiency, correct binding, thermal stability, and pH-responsiveness of individual nanostructures were prepared from non-functionalized strands to prevent aggregation mediated by hydrophobic moieties. To achieve this, all the cholesterol-functionalized oligonucleotides were replaced with non-modified strands of identical sequence.

Concentrated solutions of DNA strands in PBS were prepared by stoichiometrically mixing all the required oligonucleotides in 200 μL DNase free Eppendorf tubes. Note that, at this stage, the concentration of DNA strands was set to be 2× or 2.15× higher as compared to the final values given in Table S2, Supporting Information, to allow introduction of the M9 component of the PBM9 medium (see relevant Experimental Section

**ADVANCED
SCIENCE NEWS**

www.advancedsciencenews.com

**ADVANCED
MATERIALS**

www.advmat.de

below) and pH adjustment. Prepared mixtures were placed in a Techne TC-512 thermal cycler, heated up to 95 °C, held at this temperature for 5 min, and then cooled down to 20 °C at the rate of −0.05 °C min⁻¹ to enable nanostructure assembly.

Samples for AGE and UV melting curves of non-cholesterolized DNA structures (60 and 600 µL, 2× DNA concentration) were transferred into 1.5 mL DNase free Eppendorf tubes and mixed in equal volumes with a solution containing PBS buffer, 37.4 mM NH_4Cl, 0.2 mM $CaCl_2$, 4 mM $MgSO_4$, 0.4% w/v casamino acids (CAAs), and 0.35% w/v glucose (pH 6.54), termed PB(2×)M9, to obtain 1× DNA concentration in PBM9 medium (pH 7.00).

For the preparation of samples for DLS, UV–vis absorbance, and CD of non-functionalized DNA nanostructures, 700 µL of 2.15x concentrated solutions of assembled DNA nanostructures were placed in 50 mL centrifuge tubes (Greiner Bio-One) and supplemented with 700 µL of PB(2×)M9. Afterward, their pH was tuned with hydrochloric acid (HCl, 1 or 6 M, Sigma-Aldrich) or potassium hydroxide (KOH, 1 or 5 M, Sigma-Aldrich) solutions using a bench-top pH meter (pH 210, Hanna Instruments) equipped with a double junction pH electrode (9110DJWP, Orion). Finally, their volume was adjusted to 1500 µL by adding milli-Q water.

All the prepared samples were stored at 4 °C and used within 24 h.

Preparation of pH-Responsive Particles: DNA strands were mixed in stoichiometric ratio in PBS to the final concentration of core strands equal to 1 µM (concentrations of all the oligonucleotides are listed in Table S2, Supporting Information), in 500 µL DNase free Eppendorf tubes. The overall sample volume was set to 60 or 200 µL, depending of the annealing protocol used.

Small volumes (60 µL) of the samples used to prepare large particles (Figure 1b), were loaded into borosilicate glass capillaries (inner section of 4 mm × 0.4 mm, CM Scientific). The capillaries were previously cleaned by sonicating for 15 min once in a 2% Hellmanex III water solution (Hellma Analytics) and then twice in milli-Q water. Both ends of the capillaries were capped with mineral oil, and sealed shut and attached to microscope slides (Menzel Gläser, 24 mm × 60 mm, No. 1) with fast-drying epoxy glue (Araldite). Sealed capillaries were then placed in a custom-made Peltier-controlled water bath and heated up to 90 °C. After incubating for 30 min, the samples were cooled down to 63 °C at the rate of −0.01 °C min⁻¹ and finally brought down to 20 °C at −0.1 °C min⁻¹.

pH-responsive particles of controlled size were prepared in a custom-made Peltier-controlled aluminum chamber allowing rapid temperature changes. 200 µL volumes of the DNA strand mixtures were pipetted into ExtraSil (ES) quartz cuvettes (350 µL, 1 mm path length, 10 mm inside width, Aireka Cells) using gel-loading pipette tips (1–200 µL, 0.5 mm thick round end, RNase/DNase free, Corning). Loaded cuvettes were placed in the aluminum chamber, heated up to 90 °C and incubated for 15 min. The samples were then cooled down to 65 °C at −1 °C s⁻¹ and held at this temperature for a growth time t_g = 15, 600, or 900 s depending on the desired particle size. Subsequently, the temperature was decreased to 35 °C at −1 °C s⁻¹, held at this value for 15 min to facilitate corona formation and then further decreased to 20 °C at the same rate. The particles can be melted and re-annealed multiple times, and it was expected that one should be able to re-assemble the particles after pH-induced network formation, as long as the pH is brought back to the initial value and the DNA density is not substantially altered.

Agarose Gel Electrophoresis of Non-Functionalized DNA Motifs: AGE was used to assess the correct folding and binding of non-functionalized DNA motifs as shown in Figure S1, Supporting Infrmation.

Samples of annealed DNA nanostructures, prepared as described above, were first mixed with 4 µL of loading dye (Thermo Fisher Scientific) and then diluted in tris-borate-EDTA (TBE) buffer (pH 8.3, 89 mM tris-borate, 2 mM EDTA, Sigma-Aldrich) to the final DNA concentration of 75 ng mL⁻¹.

Agarose gels were prepared at 1.5% w/v agarose (Sigma-Aldrich) in TBE buffer supplemented with SYBR safe DNA gel stain (Invitrogen, Thermo Fisher Scientific). Wells were filled with small volumes (10 µL) of diluted samples, equivalent to 750 ng of DNA. The two outermost wells carried a 100 bp DNA reference ladder (Thermo Fisher Scientific). Gels were run for

120 min at 75 V (3 V cm⁻¹), and then imaged using a GelDoc-It imaging system.

The collected images were analyzed through a tailor-made Matlab script to obtain the integrated line intensity profiles.

DLS of Non-Cholesterolized Nanostar Structures: DLS was used to both validate the successful assembly of non-cholesterolized DNA nanostructures and examine their stability at acidic pH (see Figure S2, Supporting Information).

First, an ultra low volume quartz cuvette (ZEN2112, Malvern) was loaded with 120 µL of annealed sample in PBM9 medium with preadjusted pH that was set to either 7.0 or 4.5. Afterward, three measurements, each consisting of fifteen data runs, were taken at room temperature with a Malvern Zetasizer Nano ZSP analyzer (scattering angle fixed at 173°, 633 nm He–Ne laser).

For each of the visible bands, the hydrodynamic diameter D_H was determined by fitting the experimental data to a lognormal distribution function and then calculating the maximum of the fit, using a custom Matlab script.

UV Melting Curves of Non-Functionalized DNA Structures: UV–vis spectrophotometry was used to assess the separation of melting temperatures T_M of core-forming motifs and corona-binding domains (Figure S3, Supporting Information), required by the multistep thermal annealing process used to form core–shell particles.

Large volumes (1200 µL) of samples containing non-functionalized DNA structures, prepared according to the protocol reported above, but excluding the annealing step, were loaded into quartz cuvettes. To prevent evaporation, 300 µL of mineral oil were carefully pipetted on top of each sample before sealing the cuvettes with parafilm-wrapped poly(tetrafluoroethylene) (PTFE) stoppers.

Samples were first cooled down from 95 to 20 °C and then heated back up to 95 °C at the rate of ±0.02 °C min⁻¹ while their absorbance at 260 nm was measured on a temperature-controlled Varian Cary 50 UV–vis spectrophotometer.

T_M was determined with a custom Matlab script for both the cooling and heating ramps by fitting the upper and lower plateaus with straight lines and then computing the intersection between their median and the experimental data via interpolation.[78]

Confocal Microscopy of Large Core–Shell Particles: Confocal microscopy images of large particles (Figure 2b) were obtained with a Leica TCS SP5 laser scanning confocal microscope equipped with a HC PL APO CORR CS 40×/0.85 dry objective (Leica).

Aggregates, prepared according to the procedure described above, were extracted from the capillary by cutting open its ends with a diamond scribe, placing it in 1.5 mL DNase free Eppendorf tube containing 60 µL of PBS buffer, and spinning down with a tabletop centrifuge for ≈30 s. The sample extracted sample was then washed twice to remove the surplus corona motifs by first diluting in PBS to the total volume of 120 µL, followed by centrifugation at 420g for 30 min and supernatant replacement with fresh PBS buffer (90 µL). Washed aggregates were pipetted into silicone rubber incubation chambers (6.5 mm × 6.5 mm × 3.5 mm, Grace Biolabs FlexWells) and sealed with DNase free tape (Grace Biolabs FlexWell Seal Strips) to prevent evaporation.

For imaging, an Ar-ion laser line at 488 nm and an He–Ne line at 633 nm were used for excitation of fluorescein (core motifs) and Alexa Fluor 647 (outer corona motifs) dyes, respectively.

Assessment of I-Motif Formation with UV Absorbance: UV–vis spectrophotometry was used to characterize i-motif formation (Figure 2d).

Annealed oligonucleotide samples (1200 µL) in PBM9 medium with pre-adjusted pH were loaded into quartz cuvettes, and their absorbance at 297 nm[60,61] was measured at room temperature using the aforementioned UV–vis spectrophotometer. The tested pH ranged from 8 to 4 with steps of 0.25 points.

The transitional pH values (pK_A) were calculated with a tailor-made Matlab script as the inflection point of sigmoidal fits to the experimental data.

Assessment of I-Motif Formation with DLS: DLS measurements, performed on the Malvern Zetasizer Nano ZSP setup, were used to confirm the accurateness of the transitional pH value extracted from UV

ADVANCED
SCIENCE NEWS

www.advancedsciencenews.com

ADVANCED
MATERIALS

www.advmat.de

response curves (Figure 2d). The recorded pH-response curve is shown in Figure S4, Supporting Information.

For these experiments, 120 µL of the samples containing core and inner corona motifs in PBM9 medium with pre-adjusted pH were pipetted into an ultralow volume quartz cuvette. Three measurements, each consisting of fifteen data runs, were then taken at room temperature. The tested pH ranged from 8 to 4 with steps of 0.25 points.

The plotted D_H values were extracted from raw intensity profiles using the previously mentioned Matlab script.

Assessment of I-Motif Formation with Circular Dichroism: CD measurements, performed on a JASCO J-810 CD spectrophotometer, were used to further validate the i-motif formation upon pH decrease (Figure 2e).

First, 200 µL of highly concentrated (20 µM) samples in PBM9 medium with pH adjusted to 7.00 or 4.50 were pipetted into a 1 mm path-length, stoppered quartz cuvette. CD spectra were then acquired at room temperature in the spectral range of 210–350 nm.

pH-Triggered Particle Aggregation Assay with Epifluorescence and DDM: DDM and epifluorescence microscopy were used to assess the pH-responsiveness of the DNA particles (Figure 2g and Figure S5, Supporting Information).

Responsive (two samples) and nonresponsive (one sample) particles prepared in PBS buffer with the thermal annealing protocol described above ($t_g = 900$ s) were transferred into silicon incubation chambers and supplemented with PB(2×)M9 at 1:1 ratio to the final volume of 120 µL. The pH of two of the samples was then adjusted with HCl and KOH to 4.50 before sealing the wells with DNase free tape and imaging for 960 min at 30 min intervals. The remaining sample with responsive particles served as a control. Both high frame-rate bright-field videos (150 fps, 8 s) and epifluorescence microscopy images were recorded with a fully motorized Nikon Eclipse Ti-E inverted epifluorescence microscope, equipped with CFI Plan Apochromat λ 40×/0.95 NA dry objective (Nikon), Grasshopper3 GS3-U3-23S6M camera (Point Gray Research), and perfect focusing system (Nikon). For the epifluorescence imaging of core motifs labeled with Alexa Fluor 594, red LED illumination, and a Texas Red filter cube (Semrock) were used.

Bright-field videos were analyzed with DDM[62,63] using a custom script written in Matlab, as described in ref. [54].

Briefly, an image structure function, $\Delta I(q, \tau)$, was obtained as

$$\Delta I(q, \tau) = \langle |d(q, t_0, \tau)|^2 \rangle_{t_0} \qquad (1)$$

In Equation (1), q is the wave-vector in Fourier space and $d(q, t_0, \tau)$ is the 2D spatial Fourier transform of $d(r, t_0, \tau) = I(r, t_0 + \tau) - I(r, t_0)$, where $I(r, t_0)$ and $I(r, t_0 + \tau)$ are two video frames collected at times t_0 and $t_0 + \tau$. $\Delta I(q, \tau)$ was then fitted to[62]

$$\Delta I(q, \tau) = A(q) \left[1 - \exp\left(-D q^2 \tau\right) \right] + B(q) \qquad (2)$$

to obtain the Brownian diffusion coefficient D. A and B are functions dependent on the static scattering properties of the sample, instruments optics and camera noise.

The computed D was used to calculate the hydrodynamic radius R_H from the Stokes–Einstein equation. Note that at late times, once aggregates become too large to diffuse and/or start percolating, the extracted R_H loses its physical meaning. Despite this, all experimental data were fitted to Equation (2) for consistency.

Analysis of epifluorescence microscopy images was performed with a tailor-made Matlab script by calculating the sum of the background-subtracted pixel intensity within the observed field of view.

Particle Stability in Bacterial Growth Media: DDM was used to evaluate the stability of DNA particles after deployment in several types of commonly used bacterial growth media (Figure S6, Supporting Information).

Small volumes (60 µL) of nonresponsive particles prepared in PBS buffer using the thermal annealing protocol described above ($t_g = 600$ s) were transferred into three silicon incubation chambers. The wells were then sealed with DNase free tape and imaged by recording three high frame-rate bright-field videos (150 fps, 8 s) per sample with the previously

described Nikon Eclipse Ti-E inverted epifluorescence microscope. After 5 min, the chambers were supplemented with M9 medium (12.8 g L^{-1} Na$_2$HPO$_4$·7H$_2$O, 3 g L^{-1} KH$_2$PO$_4$, 0.5 g L^{-1} NaCl, 1 g L^{-1} NH$_4$Cl, 11 mg L^{-1} CaCl$_2$, 240 mg L^{-1} MgSO$_4$, and 0.4% w/v glucose), M63 medium (13.6 g L^{-1} KH$_2$PO$_4$, 0.5 mg L^{-1} FeSO$_4$·7H$_2$O, 0.5 g L^{-1} MgSO$_4$·7H$_2$O, 1.27 mg L^{-1} thiamine, 2.64 g L^{-1} (NH$_4$)$_2$SO$_4$, and 0.5% w/v Glucose) or M63 medium containing casamino acids (CAAs, 0.4% w/v) at 1:1 ratio to the final volume of 120 µL. After this, the wells were resealed and the samples were imaged by acquiring three high frame-rate bright-field videos per chamber at times $t = 60$, 120, 180, 300, and 1200 min from the growth medium addition.

The acquired data was analyzed using a custom DDM analysis script written in Matlab, as described in the previous section.

Bacterial Strains and Growth Conditions: All the experiments involving bacteria were carried out with the highly motile MG1655 *E. coli* strain. For fluorescence imaging (Figures 3d and 4c; Figures S10 and S16, Supporting Information), the strain was transformed with the pWR20-EGFP plasmid that enables the constitutive expression of the enhanced green fluorescent protein (EGFP) in the cytoplasm and kanamycin resistance.[79,80]

E. coli cells were grown from single colonies in 50 mL conical glass flask filled with 5 mL of LB medium (10 g L^{-1} Tryptone, 5 g L^{-1} yeast extract, 0.5 g L^{-1} NaCl) in an overnight incubation carried out at 37 °C, with continuous shaking at 220 rpm. A small volume (50 µL) of the culture in LB was then transferred into a glass flask containing 50 µL of M63 medium and the cells were allowed to grow to an optical 0.2–0.3 OD using the same incubation conditions. Before the experiments, bacteria were pelleted through centrifugation at 8000g for 2 min, washed twice with fresh buffer (PBS or PB(2×)M9) and concentrated to obtain a final OD of 0.11 after dilution by mixing all the components required to perform specific experiments. Note that to guarantee the expression of EGFP in all *E. coli*, both LB and M63 media were supplemented with kanamycin.

PBM9 Medium: The deployment of core–shell DNA particles in bacterial cultures yielded solutions that are partly made up of PBS buffer used in their production. To robustly grow bacteria in a medium that matches the ionic and buffering characteristics of PBS buffer, PBM9 (137 mM NaCl, 2.7 mM KCl, 8 mM Na$_2$HPO$_4$, 2 mM KH$_2$PO$_4$, 18.7 mM NH$_4$Cl, 0.1 mM CaCl$_2$, 2 mM MgSO$_4$, 0.2% w/v CAAs, various concentrations of glucose, pH adjusted to 7.00 with HCl and KOH) which is based on the common M9 medium was devised, with the buffering and ionic components of PBS.

The medium was used in all the experiments included in this study that involve *E. coli* and/or DNA particles/nanostructures.

Bacterial Growth and pH Changes in PBM9 Medium: OD measurements, performed on the aforementioned UV–vis spectrophotometer, were used to characterize the bacterial growth in PBM9 medium (Figure 3b). The accompanying pH changes were tracked using a bench-top pH meter. 250 µL of *E. coli* cells in LB (overnight growth) were loaded into 250 mL conical glass flasks with 24.75 mL of PBM9 medium (various glucose concentrations) and then incubated at 37 °C with continuous shaking at 220 rpm. Every 45 min, two volumes of 1 mL each were transferred into 1.5 mL Eppendorf tubes. The first sample was pipetted into a disposable cuvette (polystyrene, BRAND) and used to measure OD. After the measurement, the aliquot was transferred back into the flask. The second sample was filtered using a 0.22 µm polyethersulfone filter into 50 mL centrifuge tube to remove bacteria cells. The resultant solution was used to measure pH. The procedure described above was repeated eleven times at $t = 45$, 90, 135, 180, 225, 270, 315, 360, 405, 450, and 495 min, after which the samples were left incubating for additional 960 min with the final measurement performed at the end of incubation cycle.

Plate Reader-Based Assay of pH and Optical Density Changes Accompanying the Bacterial Growth: Turbidity and fluorescence measurements, performed on a FLUOstar Omega plate reader, were used to determine the optimal glucose concentration enabling bacteria-induced particle activation in conditions used for further experiments (Figures S7 and S8, Supporting Information).

E. coli cells were initially grown and washed as described above, then resuspended in PBS and loaded into a DNase free, flat-bottom 96-well plate (CELLSTAR Black 96 Well Cell Culture Microplates, Greiner Bio-One). Each well was then topped with 120 µL of PB(2×)M9 (various glucose

concentration) and 10 µL of fluorescein (FITC)-dextran (3 kDa, anionic, Sigma-Aldrich) solution in PBS to a total volume of 240 µL, resulting in the final FITC-dextran concentration of 50 µM and OD of 0.11. OD and fluorescence intensity at 520 nm upon excitation at 400 (I_{400}) and 485 nm (I_{485}) were measured in the plate reader for 2160 min at 8 min intervals while shaking at 700 rpm in double-orbital mode and keeping the temperature at 37 °C.

The pH was extracted from the intensity ratio I_{485}/I_{400}[81] using a calibration curve (Figure S9, Supporting Information), The calibration curve was acquired by first preparing 1 mL solutions of 50 µM FITC-dextran in PBM9 (various pH), loading 240 µL of each sample into a 96-well plate, and then measuring I_{400} and I_{485} on the plate reader at 37 °C. The pH ranged from 8 to 4 at 0.25 intervals, and was adjusted with HCl and KOH. The collected data were processed with a tailor-made Matlab script by fitting with a sigmoid function.

Bacteria Immobilization Assay: For experiments on bacteria-induced particle aggregation and subsequent *E. coli* immobilization (Figure 3d,e and Figure S11, Supporting Information), three wells in a 96-well plate were filled with 10 µL of highly concentrated *E. coli* solution in PBS (OD = 0.66 after 4× dilution), prepared as described above, 10 µL of PBS and 120 µL of PB(2×)M9 (glucose concentration set at 0.100% w/v or 0.175% w/v after dilution at 1:1 ratio). Two of the wells with different glucose content were topped with 100 µL of the PBS solution containing pH-responsive particles (t_g = 15 s), while the third well was filled with an identical volume of PBS, and used as a control. Afterward, samples were incubated in the previously introduced plate reader for t = 0, 60, 120, 180, 240, 300, 360, 420, 480, 540, 720, 900, 1080, 1260, and 1440 min at 37 °C, with shaking at 500 rpm for 30 s every 5 min. Note that a distinct set of samples was used for each time point.

All samples were imaged with the aforementioned bright-field and epifluorescence microscopy setup by taking a set of seven high frame-rate videos (150 fps, 8 s) and epifluorescence microscopy images. Green LED illumination/Texas Red filter (Semrock) and blue LED/GFP filter (Semrock) were used to record signals from core motifs (Alexa Fluor 594) and *E. coli* (EGFP), respectively.

The parameter σ, introduced in ref. [54] and used here to gauge bacterial motility (Figure 3d and Figure S11, Supporting Information), was calculated with a custom Matlab script from bright-field videos as

$$\sigma = \left\langle \sqrt{\frac{\sum_{m=-3}^{3}\left[I(n+m)-\bar{I}\right]^2}{7}} \right\rangle_n \frac{\sigma_{max}}{7} \qquad (3)$$

where $I(n)$ represents the nth frame of video, $\bar{I} = \frac{\sum_{m=-3}^{3} I(n+m)}{7}$, $\langle \cdots \rangle_n$ indicates a rolling average over the entire video, and σ_{max} is the highest intensity standard deviation value recorded in all the videos. Parameter $\bar{\sigma}$ shown in Figure 3e was computed by averaging σ over all the pixels in a frame.

Bacterial growth and pH changes occurring throughout the assay (Figure 3f and Figure S10, Supporting Information) were monitored on the plate reader with analogous samples containing non-fluorescent particles and *E.coli* lacking the pWR20-EGFP plasmid. To enable pH tracking, 10 µL of PBS were replaced with an identical volume of 1.2 mM FITC-dextran solution in PBS. Prepared samples were incubated for 1440 min at 37 °C with shaking at 500 rpm for 30 s every 5 min. OD, I_{485} and I_{400} were measured at 5 min intervals over time. The pH was then calculated from I_{485}/I_{400} using the calibration curve shown in Figure S9, Supporting Information.

Bacteria Detection with a Ratiometric pH Probe: For experiments used to sense pH changes with fluorophore-labeled particles, (Figure S12, Supporting Information), two wells in a 96-well plate were filled with 20 µL of PBS solution containing *E. coli* cells (OD = 0.66 before concentrating the cells 2×). Both chambers were then topped with 100 µL of responsive particles (t_g = 15 s) in PBS, which were formed using fluorescein-labeled core motifs, and 120 µL of PB(2×)M9 medium with different glucose concentrations (0.100% w/v or 0.175% w/v in the final solution). Two additional wells were loaded with 240 µL of equimolar particle solutions in PBM9. The pH of one of them was adjusted to 4.50 with HCl and KOH. Fluores-

cence intensities I_{400} and I_{485} were automatically measured in the aforementioned plate reader for 1440 min, at 5 min intervals, temperature set to 37 °C, with shaking at 500 rpm for 30 s every 5 min.

The recorded fluorescence intensity ratios I_{485}/I_{400} were used to calculate pH using calibration curve recorded for fluroescein-dextran probes (Figure S9, Supporting Information). The use of this calibration curve is justified by the control experiment in Figure S13, Supporting Information.

Bacteria Sensing with a Fluorophore–Quencher Pair: Fluorescence measurements used to sense bacteria-induced pH changes with particles modified with the fluorophore–quencher pair (Figure S14, Supporting Information) were carried out on the plate reader described above. Rhodamine 6G (Rh6G) and Black Hole Quencher 1 (BHQ1) were used as fluorophore and quencher, respectively.

First, small volumes (10 µL) of *E. coli* solution in PBS (4× dilution results in OD of 0.66), prepared as in the protocol described above, were loaded into four wells of a 96-well plate. Two of the chambers were then filled with 100 µL of responsive particles (t_g = 15 s, Rh6G and BHQ1) in PBS, 10 µL of *IM*-3m* (BHQ1) strand in PBS, and 120 µL of PB(2×)M9 medium. The BHQ1-modified strand was included to block any remaining sites with the Rh6G dye located within the particles' cores, that could not be accessed and quenched by inner corona motifs during particle assembly. The two remaining wells were topped with 110 µL of PBS buffer and 120 µL of PB(2×)M9 medium. The overall glucose concentration was set to 0.100% w/v or 0.175% w/v and varied between samples of the same type. In the next step, a control sample was prepared in a separate well by mixing 100 µL of PBS solution containing responsive particles (t_g = 15 s, Rh6G) with 20 µL of PBS buffer and 120 µL of PB(2×)M9 medium. All the samples were incubated in the plate reader for 1440 min at 37 °C, with shaking at 500 rpm for 30 s every 5 min. Fluorescence intensity at 530 nm upon excitation at 485 nm was monitored over time every 5 min.

The final curves representing the samples that contain both *E. coli* and particles in PBM9 medium with distinct glucose concentration, shown in Figure S14, Supporting Information, were obtained by subtracting the signal recorded from analogous samples lacking the particles. This operation was performed to eliminate contributions from *E. coli* autofluorescence, which can be detected at this wavelength.[82]

MIC Estimation Assay: The minimum inhibitory concentration (MIC) of the antibiotic ciprofloxacin was measured using the broth microdilution technique[83] on the aforementioned plate reader (Figure S15, Supporting Information).

Cells were grown in LB at 37 °C overnight with shaking at 220 rpm, and inoculated at a 1:100 dilution into a 96-well plate containing various concentrations of ciprofloxacin in PBM9, for a final volume of 200 µL. The plate was incubated for 960 min at 37 °C with 700 rpm shaking in double-orbital mode. OD was monitored over time every 13 min.

Preparation of Antibiotic-Loaded GUVs: Giant unilamellar vesicles (GUVs) with encapsulated ciprofloxacin were prepared using the emulsion-transfer method.[47,54,84] A glass vial (1.5 mL) was loaded with 500 µL of paraffin oil (Sigma-Aldrich) and 100 µL of a 10 mg mL^{-1} solution of 1,2-dioleoyl-sn-glycero-3-phosphocholine lipids (DOPC, Avanti Polar Lipids) in chloroform. Afterward, the solution was vortexed for 1 min, incubated for 60 min at ≈85 °C to evaporate chloroform, and left for 15 min to cool down to room temperature. In the next step, 250 µL of the lipid–oil solution (final lipid concentration 2 mg mL^{-1}) were pipetted into a clean 1.5 mL glass vial and mixed with 25 µL of the inside-solution (I-solution, 3.2 µg mL^{-1} ciprofloxacin and 100 µM dextran (50 kDa, Sigma-Aldrich) in PBM9 (glucose replaced with 0.333% w/v sucrose)) by vortexing for ≈1 min. The generated turbid emulsion was layered on top of 150 µL of the outside-solution (O-solution, PBM9 (0.175% w/v glucose)) in a 1.5 mL DNase free Eppendorf tube, and centrifuged at 9000*g* for 30 min. After centrifugation, first the oil and then the supernatant were removed from the sample, leaving 50 µL of O-solution containing pelleted GUVs. In the final step, the resulting solution was diluted and resuspended by adding 100 µL of fresh O-solution and gently pipetting it up and down seven to ten times.

Assessment of Antimicrobial Responses in Synthetic Cell Signaling Network Interfaced with Bacteria: To test the response of the full netosis-like pathway (Figure 4b,c and Figure S16, Supporting Information), four wells in

a 96-well plate were loaded with 10 µL of *E. coli* solution in PB(2×)M9 (OD = 0.66 before concentrating the cells 4×), prepared according to the aforementioned protocol, and 90 µL of PB(2×)M9. All the wells were then topped with 100 µL of PBS solution containing responsive or nonresponsive particles (t_g = 15 s, two wells with each particle type). Finally, 40 µL of ciprofloxacin-loaded GUVs in PBM9 were added to two wells, each carrying different particle type, while the remaining two wells were filled with an identical volume of PBM9. The overall glucose concentration in all the samples was 0.175% w/v. Prepared samples were incubated in the plate reader described above for 1440 min at 37 °C, with shaking at 500 rpm for 30 s every 5 min. OD was measured at 5 min intervals over time.

Prior to, and after incubation, all the samples were imaged with the aforementioned bright-field and epifluorescence microscopy setup. Signals from core motifs (Alexa Fluor 594) and *E. coli* (EGFP) were recorded using green LED illumination/Texas Red filter and blue LED/GFP filter, respectively.

Supporting Information

Supporting Information is available from the Wiley Online Library or from the author.

Conflict of Interest

The authors declare no conflict of interest.

Data Availability Statement

A dataset underpinning these results is freely available in Apollo, the University of Cambridge Repository, at https://doi.org/10.17863/CAM.95810.

[1] J. C. Blain, J. W. Szostak, *Annu. Rev. Biochem.* **2014**, *83*, 615.
[2] B. C. Buddingh, J. C. M. van Hest, *Acc. Chem. Res.* **2017**, *50*, 769.
[3] E. Cho, Y. Lu, *ACS Synth. Biol.* **2020**, *9*, 2881.
[4] Y. Zhu, X. Guo, J. Liu, F. Li, D. Yang, *Small Methods* **2020**, *4*, 2000406.
[5] M. A. Boyd, N. P. Kamat, *Trends Biotechnol.* **2021**, *39*, 927.
[6] A. O. Robinson, O. M. Venero, K. P. Adamala, *Curr. Opin. Chem. Biol.* **2021**, *64*, 165.
[7] S. Slomovic, K. Pardee, J. J. Collins, *Proc. Natl. Acad. Sci. USA* **2015**, *112*, 14429.
[8] Z. Chen, J. Wang, W. Sun, E. Archibong, A. R. Kahkoska, X. Zhang, Y. Lu, F. S. Ligler, J. B. Buse, Z. Gu, *Nat. Chem. Biol.* **2018**, *14*, 86.
[9] N. Krinsky, M. Kaduri, A. Zinger, J. Shainsky-Roitman, M. Goldfeder, I. Benhar, D. Hershkovitz, A. Schroeder, *Adv. Healthcare Mater.* **2018**, *7*.
[10] Y. Ding, L. E. Contreras-Llano, E. Morris, M. Mao, C. Tan, *ACS Appl. Mater. Interfaces* **2018**, *10*, 30137.
[11] O. D. Toparlak, J. Zasso, S. Bridi, M. D. Serra, P. Macchi, L. Conti, M. Baudet, S. S. Mansy, *Sci. Adv.* **2020**, *6*, eabb4920.
[12] A. Salehi-Reyhani, O. Ces, Y. Elani, *Exp. Biol. Med.* **2017**, *242*, 1309.
[13] C. Xu, S. Hu, X. Chen, *Mater. Today* **2016**, *19*, 516.
[14] T. F. Zhu, J. W. Szostak, *J. Am. Chem. Soc.* **2009**, *131*, 5705.
[15] S. Kretschmer, K. A. Ganzinger, H. G. Franquelim, P. Schwille, *BMC Biol.* **2019**, *17*, 43.
[16] J. Steinkühler, R. L. Knorr, Z. Zhao, T. Bhatia, S. M. Bartelt, S. Wegner, R. Dimova, R. Lipowsky, *Nat. Commun.* **2020**, *11*, 905.
[17] K. Y. Lee, S. Park, K. A. Lee, S. Kim, H. Kim, Y. Meroz, L. Mahadevan, K. Jung, T. K. Ahn, K. K. Parker, K. Shin, *Nat. Biotechnol.* **2018**, *36*, 530.
[18] S. Berhanu, T. Ueda, Y. Kuruma, *Nat. Commun.* **2019**, *10*, 1325.
[19] S. Deshpande, S. Wunnava, D. Hueting, C. Dekker, *Small* **2019**, *15*, 1902898.
[20] F. G. Downs, D. J. Lunn, M. J. Booth, J. B. Sauer, W. J. Ramsay, R. G. Klemperer, C. J. Hawker, H. Bayley, *Nat. Chem.* **2020**, *12*, 363.
[21] S. Zhang, C. Contini, J. W. Hindley, G. Bolognesi, Y. Elani, O. Ces, *Nat. Commun.* **2021**, *12*, 1673.
[22] V. Mukwaya, S. Mann, H. Dou, *Commun. Chem.* **2021**, *4*, 161.
[23] J. M. Smith, R. Chowdhry, M. J. Booth, *Front. Mol. Biosci.* **2022**, *8*, 809945.
[24] J. Garamella, S. Majumder, A. P. Liu, V. Noireaux, *ACS Synth. Biol.* **2019**, *8*, 1913.
[25] W. T. Kaufhold, R. A. Brady, J. M. Tuffnell, P. Cicuta, L. Di Michele, *Bioconjugate Chem.* **2019**, *30*, 1850.
[26] A. Samanta, V. Sabatino, T. R. Ward, A. Walther, *Nat. Nanotechnol.* **2020**, *15*, 914.
[27] A. Leathers, M. Walczak, R. A. Brady, A. Al Samad, J. Kotar, M. J. Booth, P. Cicuta, L. Di Michele, *J. Am. Chem. Soc.* **2022**, *144*, 17468.
[28] R. Rubio-Sánchez, S. E. Barker, M. Walczak, P. Cicuta, L. Di Michele, *Nano Lett.* **2021**, *21*, 2800.
[29] Y. Elani, R. V. Law, O. Ces, *Phys. Chem. Chem. Phys.* **2015**, *17*, 15534.
[30] P. van Nies, I. Westerlaken, D. Blanken, M. Salas, M. Mencia, C. Danelon, *Nat. Commun.* **2018**, *9*, 1583.
[31] E. Rideau, R. Dimova, P. Schwille, F. R. Wurm, K. Landfeste, *Chem. Soc. Rev.* **2018**, *47*, 8572.
[32] P. Stano, *Chem. Eur. J.* **2019**, *25*, 7798.
[33] H. Niederholtmeyer, C. Chaggan, N. K. Devaraj, *Nat. Commun.* **2018**, *9*, 5027.
[34] X. Huang, M. Li, D. C. Green, D. S. Williams, A. J. Patil, S. Mann, *Nat. Commun.* **2013**, *4*, 2239.
[35] A. Joesaar, S. Yang, B. Bögels, A. van der Linden, P. Pieters, B. V. V. S. P. Kumar, N. Dalchau, A. Phillips, S. Mann, T. F. A. de Greef, *Nat. Nanotechnol.* **2019**, *14*, 369.
[36] A. F. Mason, J. C. M. van Hest, *Emerg. Top. Life Sci.* **2019**, *3*, 567.
[37] M. E. Allen, J. W. Hindley, D. K. Baxani, O. Ces, Y. Elani, *Nat. Rev. Chem.* **2022**, *6*, 562.
[38] C. Xu, N. Martin, M. Li, S. Mann, *Nature* **2022**, *609*, 1029.
[39] R. Rubio-Sánchez, G. Fabrini, P. Cicuta, L. Di Michele, *Chem. Commun.* **2021**, *57*, 12725.
[40] J. S. Marshall, R. Warrington, W. Watson, H. L. Kim, *Allergy Asthma Clin. Immunol.* **2018**, *14*, 49.

[41] M. S. Diamond, T. Kanneganti, *Nat. Immunol.* **2022**, *23*, 165.

[42] B. Lim, Y. Yin, H. Ye, Z. Cui, A. Papachristodoulou, W. E. Huang, *ACS Synth. Biol.* **2022**, *11*, 1349.

[43] P. M. Gardner, K. Winzer, B. G. Davis, *Nat. Chem.* **2009**, *1*, 377.

[44] R. Lentini, S. Perez Santero, F. Chizzolini, D. Cecchi, J. Fontana, M. Marchioretto, C. Del Bianco, J. L. Terrell, A. C. Spencer, L. Martini, M. Forlin, M. Assfalg, M. Dalla Serra, W. E. Bentley, S. S. Mansy, *Nat. Commun.* **2014**, *5*, 4012.

[45] M. Schwarz-Schilling, L. Aufinger, A. Mückl, F. C. Simmel, *Integr. Biol.* **2016**, *8*, 564.

[46] R. Lentini, N. Y. Martín, M. Forlin, L. Belmonte, J. Fontana, M. Cornella, L. Martini, S. Tamburini, W. E. Bentley, O. Jousson, S. S. Mansy, *ACS Cent. Sci.* **2017**, *3*, 117.

[47] G. Rampioni, F. D'Angelo, M. Messina, A. Zennaro, Y. Kuruma, D. Tofani, L. Leoni, P. Stano, *Chem. Commun.* **2018**, *54*, 2090.

[48] X. Wang, L. Tian, H. Du, M. Li, W. Mu, B. W. Drinkwater, X. Han, S. Mann, *Chem. Sci.* **2019**, *10*, 9446.

[49] J. M. Smith, D. Hartmann, M. J. Booth, bioRxiv **2022**, https://doi.org/10.1101/2022.07.22.500923.

[50] I. Gispert, J. W. Hindley, C. P. Pilkington, H. Shree, L. M. C. Barter, O. Ces, Y. Elani, *Proc. Natl. Acad. Sci. USA* **2022**, *119*, e2206563119.

[51] V. Brinkmann, U. Reichard, C. Goosmann, B. Fauler, Y. Uhlemann, D. S. Weiss, Y. Weinrauch, A. Zychlinsky, *Science* **2004**, *303*, 1532.

[52] M. J. Kaplan, M. Radic, *J. Immunol.* **2012**, *189*, 2689.

[53] V. Papayannopoulos, *Nat. Rev. Immunol.* **2018**, *18*, 134.

[54] M. Walczak, R. A. Brady, L. Mancini, C. Contini, R. Rubio-Sánchez, W. T. Kaufhold, P. Cicuta, L. Di Michele, *Nat. Commun.* **2021**, *12*, 4743.

[55] R. Sánchez-Clemente, M. I. Igeño, A. G. Población, M. I. Guijo, F. Merchán, R. Blasco, *Proceedings* **2018**, *2*, 1297.

[56] R. A. Brady, N. J. Brooks, P. Cicuta, L. Di Michele, *Nano Lett.* **2017**, *17*, 3276.

[57] R. A. Brady, N. J. Brooks, V. Fodera, P. Cicuta, L. Di Michele, *J. Am. Chem. Soc.* **2018**, *140*, 15384.

[58] R. A. Brady, W. T. Kaufhold, N. J. Brooks, V. Fodera, L. Di Michele, *J. Phys.: Condens. Matter* **2019**, *31*, 074003.

[59] W. Shu, D. Liu, M. Watari, C. K. Riener, T. Strunz, M. E. Welland, S. Balasubramanian, R. A. McKendry, *J. Am. Chem. Soc.* **2005**, *127*, 17054.

[60] Z. Dvořáková, D. Renčiuk, I. Kejnovská, P. Školáková, K. Bednářová, J. Sagi, M. Vorlíčková, *Nucleic Acids Res.* **2018**, *46*, 1624.

[61] P. Školáková, D. Renčiuk, J. Palacký, D. Krafčík, Z. Dvořáková, I. Kejnovská, K. Bednářová, M. Vorlíčková, *Nucleic Acids Res.* **2019**, *47*, 2177.

[62] R. Cerbino, V. Trappe, *Phys. Rev. Lett.* **2008**, *100*, 188102.

[63] R. Cerbino, P. Cicuta, *J. Chem. Phys.* **2017**, *147*, 110901.

[64] I. V. Nesterova, E. E. Nesterov, *J. Am. Chem. Soc.* **2014**, *136*, 8843.

[65] N. Chen, N. Du, W. Wang, T. Liu, Q. Yuan, Y. Yang, *Angew. Chem., Int. Ed.* **2022**, *61*, e202115572.

[66] L. Wang, X. Zhang, C. Tang, P. Li, R. Zhu, J. Sun, Y. Zhang, H. Cui, J. Ma, X. Song, W. Zhang, X. Gao, X. Luo, L. You, Y. Chen, Z. Dai, *Nat. Commun.* **2022**, *13*, 3879.

[67] S. Balasubramanian, M.-E. Aubin-Tam, A. S. Meyer, *ACS Synth. Biol.* **2019**, *8*, 1564.

[68] T. Yamashita, R. Yamamoto-Ikemoto, *Int. J. Environ. Res. Public Health* **2014**, *11*, 9835.

[69] P. Van Dillewijn, H. Nojiri, J. R. Van Der Meer, T. K. Wood, *Microb. Biotechnol.* **2009**, *2*, 125.

[70] A. Rodrigo-Navarro, S. Sankaran, M. J. Dalby, A. del Campo, M. Salmeron-Sanchez, *Nat. Rev. Mater.* **2021**, *6*, 1175.

[71] Z. Ming, L. Han, M. Bao, H. Zhu, S. Qiang, S. Xue, W. Liu, *Adv. Sci.* **2021**, *8*, 2102545.

[72] S. Bhusari, S. Sankaran, A. del Campo, *Adv. Sci.* **2022**, *9*, 2106026.

[73] Y. Hu, D. Zhao, X. Yu, Y. Hu, R. Li, M. Ge, T. Xu, X. Liu, H. Liao, *Front. Microbiol.* **2017**, *8*, 82.

[74] M. Y. Memar, H. B. Baghi, *Biomed. Pharmacother.* **2019**, *111*, 649.

[75] B. M. Mognetti, P. Cicuta, L. Di Michele, *Rep. Prog. Phys.* **2019**, *82*, 116601.

[76] D. Morzy, R. Rubio-Sánchez, H. Joshi, A. Aksimentiev, L. Di Michele, U. F. Keyser, *J. Am. Chem. Soc.* **2021**, *143*, 7358.

[77] J. N. Zadeh, C. D. Steenberg, J. S. Bois, B. R. Wolfe, M. B. Pierce, A. R. Khan, R. M. Dirks, N. A. Pierce, *J. Comput. Chem.* **2011**, *32*, 170.

[78] J. L. Mergny, L. Lacroix, *Oligonucleotides* **2003**, *13*, 515.

[79] N. Lord, Ph.D. Thesis, Harvard University, Cambridge, MA **2014**.

[80] L. Mancini, G. Terradot, T. Tian, Y. Pu, Y. Li, C. J. Lo, F. Bai, T. Pilizota, *Biophys. J.* **2020**, *118*, 4.

[81] G. R. Bright, G. W. Fisher, J. Rogowska, D. L. Taylor, *J. Cell Biol.* **1987**, *104*, 1019.

[82] J. Surre, C. Saint-Ruf, V. Collin, S. Orenga, M. Ramjeet, I. Matic, *Sci. Rep.* **2018**, *8*, 12088.

[83] I. Wiegand, K. Hilpert, R. E. W. Hancock, *Nat. Protoc.* **2011**, *3*, 163.

[84] S. Fujii, T. Matsuura, T. Sunami, T. Nishikawa, Y. Kazuta, T. Yomo, *Nat. Protoc.* **2014**, *9*, 1578.